

Signals induced in semiconductor gamma-ray imaging detectors

J. D. Eskin,^{a)} H. H. Barrett, and H. B. Barber

The University of Arizona, Optical Sciences Center and Department of Radiology, Tucson, Arizona 85724

(Received 24 July 1997; accepted for publication 6 October 1998)

The signal induced in a readout circuit connected to a pixel electrode in a semiconductor gamma-ray imaging array is calculated by solving the Laplace equation. Two approaches are presented that use Green functions in solving the boundary value problem: decomposition into basis functions, and construction of an infinite series of image charges. Another approach is developed based on the Ramo–Shockley theorem, which makes use of weighting potentials. These potentials may be readily calculated in three dimensions using a Fourier-transform propagation technique. An analytic solution is found for the special two-dimensional case of a strip detector. Experiments on CdZnTe square-pixel test structures using alpha radiation confirm the expected trends in pulse shape as a function of pixel size. Signals observed simultaneously on adjacent pixels also follow the predicted division of currents. Trends with pixel size are also confirmed in the shape of pulse-height spectra taken using a ^{99m}Tc source. © 1999 American Institute of Physics. [S0021-8979(99)03302-2]

I. INTRODUCTION

Gamma-ray imaging detectors based on compound semiconductors such as Cd_xZn_{1-x}Te are poised to become important tools in nuclear medicine,¹ astrophysics,^{2,3} and other fields, providing higher spatial resolution and higher-energy resolution than can be obtained with scintillator-based gamma cameras. These detector arrays are made from slabs of single-crystal semiconductor material with individual pixels defined either by square regions patterned into the electrode on one side of the slab, or by a crossed-stripe pattern formed on opposing sides. The detector volume is a region of intrinsic material or a fully depleted *p-i-n* structure which operates under a bias voltage in photoconductive mode. Gamma rays absorbed in a photoelectric interaction produce mobile electron–hole pairs, which move under the applied field, inducing a current in nearby pixel electrodes. A readout circuit connected to each detector element responds to the integrated current resulting from a single gamma interaction. The integrated signal corresponds to the energy of the gamma ray, and this pulse height is used in spectroscopic analysis to screen out events of interest for imaging.

In single-element semiconductor detectors, the induced signal is proportional to the distance the charge carriers move. Strong trapping of holes relative to electrons results in signals that vary with depth of interaction and a pulse-height spectrum having a characteristic trapping tail (as discussed in more detail later in the article). In multielement detectors, the induced current no longer depends only on the distance that carriers travel, but also on their proximity to the sensing electrode. This “near-field” effect can be exploited by choosing the pixel plane to be the anode and making the pixel dimensions small in comparison with the detector thickness. In this situation, the signal is due almost entirely to electron transport, and the hole trapping tail is largely

eliminated, with no loss in detection efficiency. However, even an infinitesimal pixel would not have the best transport properties. Electron-only transport does involve some variation in signal with depth of interaction, and some component of hole transport can serve to balance out this trend. Another aspect of small pixels is that they are prone to degradation of the energy resolution by a variety of mechanisms such as escape of *K*-shell x rays, straggle of energetic electrons, Compton scattering, and diffusion of charge carriers. In practice, these processes of nonlocal charge deposition set a lower bound on pixel size, unless steps are taken in the image-acquisition system to recover a signal that has spread to neighbor pixels.⁴ For a given set of material parameters and energy of incident radiation, there is an optimal pixel aspect ratio, which may be determined by modeling both the induced signals and the scattering processes.

In Sec. II we derive expressions for the induced signal by solving the three-dimensional Laplace equation. In Sec. III two forms of a Green function are developed: an expansion into basis functions, and a summation of a series of image charges. In Sec. IV approaches using the Ramo–Shockley theorem are presented. The three approaches to calculating the induced signal produce equivalent results, but one may have a computational advantage over another when analyzing a given detector geometry. Section V discusses the effect of carrier trapping and methods for calculating the induced signal from the charge distribution. Section VI presents an analysis of the effect of pixel size on the detected signal. Section VII presents experimental results that confirm the predicted trends in temporal pulse shapes and pulse-height spectra.

II. INDUCED CURRENTS IN MULTIELEMENT DETECTORS

We consider the detector array geometry shown in cross section in Fig. 1. The continuous top electrode is held at a (negative) bias potential V_b , while the bottom pixel electrodes are kept at ground potential by a transimpedance am-

^{a)}Currently with Panoptic Vision, Inc., Boulder, CO 80303; electronic mail: josh@pancam.com

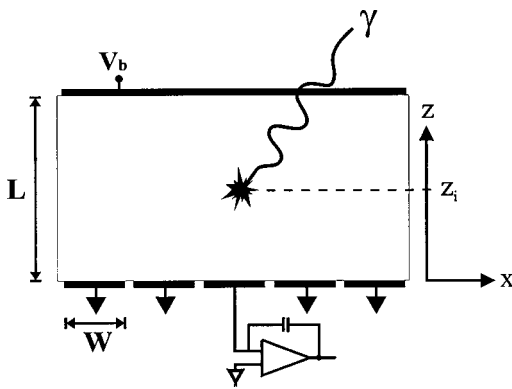


FIG. 1. Detector in cross section. The continuous top electrode is connected to a bias voltage V_b . Pixel electrodes on the bottom plane are held at ground potential by the input node of a charge-sensitive preamplifier.

plifier connected to each pixel. When a gamma ray is absorbed in a photoelectric interaction, a cloud of many thousand electron-hole pairs is created. Under the influence of the bias field, the holes will drift upward toward the continuous (cathode) electrode while the electrons will drift downward toward the more positive (anode) pixel electrodes. The volume of the detector consists of an intrinsic (or well-compensated) semiconductor or a depletion region having very high resistivity, and it is assumed to be free of charge carriers except for those liberated in an interaction with a gamma ray. Thermally generated charges do exist in the volume and result in a low-level dark current, which can be considered to be independent of the pulse of current resulting from a gamma-ray interaction.

In doped semiconductors, or in ionic materials, compensating charges move to surround mobile charges, effectively screening their fields from being sensed at macroscopic distances. Since charge neutrality is maintained at all points in the detector volume, no electrode currents are observed until moving carriers actually reach the electrodes. By contrast, in an insulating medium, currents resulting from introduction of mobile carriers into the medium are due entirely to induction. Unlike the case of doped semiconductors or conductive Ohmic media, there is no reservoir of free carriers available to surround drifting carriers and maintain local charge neutrality, at least not on the time scale of interest. The characteristic relaxation time of a medium is given by $\tau_R = \rho\epsilon$, where ρ is the resistivity, and $\epsilon = \epsilon_r\epsilon_0$ is the dielectric constant of the material. For a typical slab of detector-grade CdZnTe having a resistivity of $5 \times 10^{10} \Omega \text{ cm}$ and a relative dielectric constant of 11, the relaxation time is 49 ms, which is long compared to typical hole drift times for these detectors of one or two microseconds. On the other hand, the charges do not move so fast (10^7 cm/s is the terminal velocity at room temperature) that electromagnetic forces need to be taken into account, so the system can be treated quasi-statically.

When a charge packet is introduced into the medium it will induce a surface charge on any nearby electrodes. As the charge packet drifts under the influence of the bias voltage, the surface charge density will change in form, starting out as nearly uniform when the charge packet is far from the

electrode. As the packet of carriers moves close to the electrode, the surface charge becomes more concentrated around the point closest to the packet. The temporal change in surface charge, integrated over the electrode area, manifests as a current flowing through the electrode. When the charge packet drifts all the way to an electrode, the mobile charges recombine with the surface charges of the opposite sign. The current pulse that should result from the sudden change in surface charge is exactly balanced by the transfer of mobile carriers into the electrode material. The net result is that there is no associated pulse of current when a charge packet reaches the electrode.

A. Single and multielement detectors

In semi-insulating media, therefore, the electrode currents may be calculated by observing the change in surface charges as carriers move inside the detector volume. However, in the case of single-element detectors, which have a continuous electrode on either side, the form of the induced currents may be found by a much simpler calculation.

The power required to move a packet of charge q at a velocity v in the direction of a field \mathcal{E} is $P = q\mathcal{E}v$. This power must be drawn from the power supply, which keeps the bias voltage $V = \mathcal{E}L$ constant across the detector thickness L . This power may be factored into a current and a voltage, $P = iV$. The current, $i = qv/L$, flows as long as there are mobile charges in the medium, regardless of their position. We separate the charge packet into electrons, $-eN_e(t)$, and holes, $eN_h(t)$, each of which moves at its own velocity (in opposite directions) and whose number may change in time. The electrode current for a single-element detector is then

$$i(t) = \frac{e}{L} [N_e(t)v_e + N_h(t)v_h]. \quad (1)$$

The electronic circuits that sense the current pulses in gamma detectors are typically configured as integrators, yielding a signal proportional to the charge stored on an integrating capacitor. If the integration time is long enough that all carriers have drifted to their respective electrodes, or have become trapped along the way, the net charge is a function of interaction depth z_i ,

$$Q(z_i) = \frac{eN_e\lambda_e}{L} \left[1 - \exp\left(-\frac{z_i}{\lambda_e}\right) \right] + \frac{eN_h\lambda_h}{L} \left[1 - \exp\left(-\frac{L-z_i}{\lambda_h}\right) \right], \quad (2)$$

where λ_e and λ_h are the mean-drift lengths for electrons and holes. Equation (2), which is known as the Hecht relation,⁵ is usually sufficient to describe the behavior of single-element detectors.

The position-independent model of current flow from Eq. (1) cannot be applied to multiple-element detectors as there are several paths the current can take, and the current through each electrode depends on the position of the carriers. We can develop a more general theory of induced currents by first considering a point charge created within the detector volume at the three-dimensional position vector \mathbf{r}_i .

In the absence of boundary conditions, the potential from this point charge follows a $|\rho - \rho_0|^{-1}$ falloff. At the pixel plane, where all electrodes are held at ground potential, a surface charge will develop to offset the discontinuity in potentials. By Gauss's law, the surface charge on the electrode is

$$\sigma(\mathbf{r}, t) = \epsilon \left. \frac{\partial \Phi(\rho, t)}{\partial z} \right|_{z=0}, \quad (3)$$

where \mathbf{r} is the two-dimensional position vector on the electrode surface, Φ is the potential within the volume, and $\epsilon = \epsilon_0 \epsilon_r$ is the permittivity of the semiconductor material. The current flowing through the pixel electrode at a given time is the time derivative of the surface charge density, integrated over the pixel area,

$$i_{\text{pix}}(t) = \int_{\text{pix}} d^2 r \frac{\partial \sigma(\mathbf{r}, t)}{\partial t}. \quad (4)$$

Often we are not interested in the details of the current flow, but need only to know the integrated charge stored on the feedback capacitor in the readout preamplifier after all carriers have had time to drift across the detector (if not trapped along the way). This charge signal depends on the initial and final surface charge densities,

$$Q_{\text{pix}} = \int_{\text{pix}} d^2 r [\sigma(\mathbf{r}, t_{\text{max}}) - \sigma(\mathbf{r}, 0)]. \quad (5)$$

Here, t_{max} is the maximum time for carriers of either sign to drift from the interaction point \mathbf{r}_i to the electrodes. As mentioned above, there is a change in surface charge as each carrier that was not trapped along the way recombines at the electrode, but no net current results. The integrated charge signal Q_{pix} generally (but not always) rises monotonically from time 0 to time t_{max} , then stays fixed until reset electronically (or further increased by detrapping carriers). The initial surface charge $\sigma(\mathbf{r}, 0)$ may be presumed to be zero, the pixel electrode voltage having been reset by its readout circuit. Even immediately after a gamma-ray absorption, the electrons and holes created will be in close proximity to each other, and there will be no effective charge distribution in the bulk until the carriers start to separate. The net signal may then be expressed using Eq. (3) as

$$Q_{\text{pix}} = \int_{\text{pix}} d^2 r \epsilon \left. \frac{\partial \Phi(\rho, t_{\text{max}})}{\partial z} \right|_{z=0}. \quad (6)$$

The key to finding the final integrated charge is to find a potential due to a single point charge which satisfies the inhomogeneous Poisson equation with the appropriate boundary conditions. Such a potential is a Green function, and methods for finding the form of this function are discussed in the next section. From the known potential the surface charge can be found from Eq. (3), and the integrated charge from Eq. (5). The solution for a general initial distribution of charge $\rho(\rho, t)$ can be found by superimposing the solutions for a distribution of point charges, under the approximation that the point charges do not interact with each other.

III. SOLUTIONS USING GREEN FUNCTIONS

The potential distribution Φ throughout the detector volume due to a charge distribution ρ satisfies the inhomogeneous Poisson equation

$$\nabla^2 \Phi(\rho, t) = \frac{-\rho(\rho, t)}{\epsilon}. \quad (7)$$

The potential can be found with the aid of a Green function $G(\rho, \rho_0)$, which represents the potential at ρ due to a point charge at ρ_0 . The function G must satisfy

$$\nabla^2 G(\rho, \rho_0) = -4\pi \delta(\rho - \rho_0), \quad (8)$$

within the volume V as well as surface boundary conditions on the top and bottom electrodes,

$$G(x, y, L) = G(x, y, 0) = 0. \quad (9)$$

We apply Green's theorem over the detector volume V , whose x and y dimensions extend to infinity. The surface S consists of the top and bottom electrodes. The outward-directed normal derivative $\partial/\partial n$ points in the $+z$ direction for the top surface at $z=L$ and the $-z$ direction for the bottom surface, where $z=0$. The small spaces that must, in practice, separate a pixel electrode from the surrounding surface region are ignored for the moment, but will be treated in the next section. When the surface boundary conditions,

$$\Phi(x, y, L) = V_B \quad \text{and} \quad \Phi(x, y, 0) = 0, \quad (10)$$

are applied, the potential is given by⁶

$$\begin{aligned} \Phi(\rho, t) = & -\frac{V_B}{4\pi} \int_{\infty} d^2 r_0 \left. \frac{\partial G(\rho, \rho_0)}{\partial z_0} \right|_{z=L} \\ & + \frac{1}{4\pi \epsilon_0 \epsilon_r} \int_V d^3 \rho_0 G(\rho, \rho_0) \rho(\rho_0, t). \end{aligned} \quad (11)$$

The first term in Eq. (11) represents the potential due to the fixed bias voltage while the second term gives the potential due to the mobile distribution of charges produced in a gamma-ray interaction. To calculate the signal induced on a pixel by a charge distribution within the detector volume, we substitute the second term in Eq. (11) into Eq. (6) to obtain

$$Q_{\text{pix}} = \frac{1}{4\pi} \int_{\text{pix}} d^2 r \frac{\partial}{\partial z} \left[\int_V d^3 \rho_0 G(\rho, \rho_0) \rho(\rho_0, t_{\text{max}}) \right] \Bigg|_{z=0}. \quad (12)$$

A. Eigenfunction solution

We present two techniques for finding the form of the Green function. One method involves constructing the Green function from an orthonormal set of basis functions that satisfy the boundary conditions. A second technique is to construct an infinite series of image charges, alternating positive and negative, arrayed in a way that the potential adds up to zero on both the top and bottom electrodes. The image-charge form of a Green function will be shown in the next section.

The needed Green function can be constructed from a complete, orthonormal set of eigenfunctions, $\{u_n\}$, that satisfy the same Dirichlet boundary conditions as Eq. (9),

$$G(\boldsymbol{r}, \boldsymbol{r}_0) = -4\pi \sum_n \frac{1}{\lambda_n} u_n(\boldsymbol{r}) u_n^*(\boldsymbol{r}_0). \tag{13}$$

To find the form of the basis functions we observe that the detector volume is assumed infinite in x and y , so complex exponentials indexed by the continuous variables ξ and η can be used in these dimensions. In the z direction, the finite extent and boundary conditions at the surfaces dictate a series of sines, indexed by the integer variable m . The form of the basis functions is then

$$u_{m\xi\eta}(x, y, z) = \sqrt{\frac{2}{L}} \sin\left(\frac{m\pi z}{L}\right) e^{2\pi i \xi x} e^{2\pi i \eta y}. \tag{14}$$

The constants in front were found by normalizing. The eigenvalues are given by

$$\lambda_m(\xi, \eta) = -\left(\frac{m\pi}{L}\right)^2 - 4\pi^2(\xi^2 + \eta^2). \tag{15}$$

Applying a formula from integral tables and substituting in the rest of the expression for G , we obtain (Ref. 6, p. 131),

$$G(\boldsymbol{r}, \boldsymbol{r}_0) = \frac{4}{L} \sum_{m=1}^{\infty} K_0\left(\frac{m\pi|\boldsymbol{r}-\boldsymbol{r}_0|}{L}\right) \sin\left(\frac{m\pi z}{L}\right) \sin\left(\frac{m\pi z_0}{L}\right), \tag{16}$$

where K_0 is the zero-order modified Bessel function. The cylindrical symmetry of G is reasonable in this geometry. We would expect that the potential at location \boldsymbol{r} due to a point source at \boldsymbol{r}_0 within the detector would depend in some detailed way on the vertical coordinates z and z_0 , but in the horizontal plane would depend only on the relative radial separation $|\boldsymbol{r}-\boldsymbol{r}_0|$.

B. Image-charge solution

The solution for G derived above is difficult to evaluate in practice. The series is an alternating one that must be coerced into convergence by means of apodizing functions. An expression for G as an infinite series of image charges converges monotonically, although not rapidly, and has the advantage of being easy to visualize as a series of real point charges. We write the Green function with positive and negative charges balanced in pairs,⁷ which serves to speed convergence of the series,

$$G(\boldsymbol{r}, \boldsymbol{r}_0) = \sum_{k=-\infty}^{\infty} \left[\frac{1}{[(2kL - z + z_0)^2 + r^2]^{1/2}} - \frac{1}{[(2kL - z - z_0)^2 + r^2]^{1/2}} \right]. \tag{17}$$

This image charge solution can be shown to be equivalent to the eigenfunction version derived above using the Poisson summation formula.⁸

With an expression for the Green function in hand, the induced signal may be calculated using Eq. (12). The expression can be simplified by evaluating the derivative with respect to z at $z=0$,

$$Q_{\text{pix}} = \sum_{k=-\infty}^{\infty} \frac{e}{4\pi} \int_{\text{pix}} d^2r \int_V d^3\boldsymbol{r}_0 \left\{ \frac{2kL + z_0}{[(2kL + z_0)^2 + r^2]^{3/2}} - \frac{2kL - z_0}{[(2kL - z_0)^2 + r^2]^{3/2}} \right\} \rho(\boldsymbol{r}_0, t_{\text{max}}). \tag{18}$$

We will find it useful to calculate the induced signal when the charge distribution is restricted to a thin vertical line which is centered over a circular pixel of radius R . In this case, the expression reduces to

$$Q_{\text{pix}} = \sum_{k=-\infty}^{\infty} \frac{e}{2} \int_0^L dz_0 \left\{ 2 - \frac{2kL + z_0}{[(2kL + z_0)^2 + R^2]^{1/2}} - \frac{2kL - z_0}{[(2kL - z_0)^2 + R^2]^{1/2}} \right\} \rho(z_0, t_{\text{max}}). \tag{19}$$

From this form for the induced signal, the signal for arbitrary pixel shapes and charge distributions can be found (Ref. 8, p. 111).

IV. SOLUTIONS USING WEIGHTING POTENTIALS

Ramo proved a theorem,⁹ introduced by Shockley,¹⁰ which provides a convenient way to calculate the current flowing through an electrode due to motion of a charge carrier. The Ramo–Shockley theorem concerns a volume within which an arbitrary number of electrodes are held at fixed potentials, and a point charge of strength e moves along a velocity vector \boldsymbol{v} . The forces that cause the charge to move are not considered here, only the fact that the charge is moving. The current flowing through a given electrode can be found by calculating a *weighting field*, \mathcal{E}_w , which is the electric field appearing within the volume if the electrode of interest is raised to unit potential and all other electrodes kept at ground potential. Then, the electrode current due to a charge at point \boldsymbol{r} is^{9,10}

$$i = e\boldsymbol{v}(\boldsymbol{r}) \cdot \mathcal{E}_w(\boldsymbol{r}). \tag{20}$$

Similarly, the integral of the electrode current can be found by means of a *weighting potential*, Φ_w . The right side of Eq. (20) is the time derivative of $-e\Phi_w(\boldsymbol{r})$, so as the point charge moves from position \boldsymbol{r}_1 to \boldsymbol{r}_2 , the net charge built up on an integrating capacitor connected to the electrode will be

$$Q = e[\Phi_w(\boldsymbol{r}_2) - \Phi_w(\boldsymbol{r}_1)]. \tag{21}$$

Here, we give a brief derivation of the Ramo–Shockley theorem. Let S_A represent the pixel of interest, S_B represent the union of all other electrodes in the region, and S_e represent a small surface surrounding a test charge e . We wish to answer the questions: how much charge Q_A is induced on electrode A due to the presence of e , and how much current i_A flows in electrode A when the charge moves? First, we consider the case in which all electrodes are held at ground potential. An electrostatic potential Φ exists throughout the volume due to the test charge e , but is forced to zero at the electrodes. The potential satisfies the Laplace equation, $\nabla^2\Phi = 0$, in the charge-free region between electrodes. When

a small sphere S_e is drawn around point e , the potential on this sphere is Φ_e . Gauss's law gives the relation between this potential and the enclosed charge,

$$\int_{S_e} d^2r \frac{\partial \Phi_e}{\partial n} = \frac{-e}{\epsilon}. \quad (22)$$

Now, we consider the case in which the charge e has been removed and electrode A has been raised to unit potential. The potential now on the surface S_e is labeled Φ'_e . We use Green's theorem to obtain a relation between Φ and Φ' , which reduces to

$$0 = \int_{S_A} d^2r \frac{\partial \Phi}{\partial n} + \Phi'_e \int_{S_e} d^2r \frac{\partial \Phi}{\partial n} - \Phi_e \int_{S_e} d^2r \frac{\partial \Phi'}{\partial n}. \quad (23)$$

By Gauss's law, these three surface integrals yield the enclosed charge, as in Eq. (22). The first integral gives the induced charge on electrode A ($-Q_A/\epsilon$). The second term gives $-\Phi'_e e/\epsilon$. The third integral is zero since there is no charge present when Φ' is applied. The result is

$$Q_A = -e\Phi'_e. \quad (24)$$

Generalizing from a point charge to a distribution of charge $\rho(\mathbf{r})$ (and dropping the minus sign), we have

$$Q_A = \int d^3r \Phi_w(\mathbf{r}) \rho(\mathbf{r}), \quad (25)$$

where Φ'_e has been renamed as Φ_w . To obtain an expression for the current flowing through electrode A as the charge moves, we take the time derivative of Eq. (24),

$$i_A = \frac{dQ_A}{dt} = -e \frac{d\Phi'_e}{dt} = -e \nabla \Phi' \cdot \frac{d\mathbf{r}}{dt}. \quad (26)$$

We define the *weighting field*, $\mathcal{E}_w = -\nabla \Phi_w$, and the velocity of the charge $\mathbf{v} = d\mathbf{r}/dt$, which results in Eq. (20). Or, if the field and velocity point in the same direction,

$$i_A = e v \mathcal{E}_w, \quad (27)$$

which is the usual statement of the Ramo-Shockley theorem.

Note that a weighting potential is not a true, dimensionally correct potential. Rather, it is a normalized quantity representing the charge induced on an electrode resulting from the introduction of a point charge into the detector volume. There are many ways to find the form of the weighting potential, one of which is to use the same Green functions derived above. The relationship between the two expressions, for the case in which the electrode of interest lies in the x - y plane, can be found by evaluating the general expression for the pixel signal, Eq. (12), for the case where the charge distribution consists of a single-carrier e located at position \mathbf{r}_0 . Comparison with Eq. (24) yields

$$\Phi_w(\mathbf{r}_0) = \frac{-1}{4\pi} \int_{\text{pix}} d^2r \frac{\partial G(\mathbf{r}, \mathbf{r}_0)}{\partial z} \Big|_{z=0}. \quad (28)$$

The usefulness of the weighting-potential approach lies in the variety of other techniques for finding potential distributions that can be applied to finding the form of $\Phi_w(\mathbf{r})$. For two-dimensional problems and simple electrode geometry,

the technique of conformal transformations can be used.^{11,12} A powerful method suitable to modeling many electrode geometries involves calculating the solid angle subtended by an infinite series of images of the electrode.¹³ Arbitrarily complex three-dimensional geometries can be evaluated using finite-element techniques.¹⁴ The planar detector geometries considered here are particularly suited to a method of finding the potential distribution from the value on one surface of the detector using a Fourier-transform propagation technique.

A. Fourier-transform propagation method

From the known potential distribution on the pixel plane (at $z=0$) and on the continuous top electrode ($z=L$), it is possible to find the potential distribution $\Phi(x, y, z)$ throughout the detector volume. Here, we follow the derivation used by Kavadias *et al.*¹⁵ Starting with a potential distribution that satisfies the Laplace equation,

$$\left(\frac{\partial^2}{\partial x^2} + \frac{\partial^2}{\partial y^2} + \frac{\partial^2}{\partial z^2} \right) \Phi(x, y, z) = 0, \quad (29)$$

we apply a *two-dimensional* Fourier transform in x and y only,

$$\int_{-\infty}^{\infty} dx dy \left(\frac{\partial^2}{\partial x^2} + \frac{\partial^2}{\partial y^2} \right) \Phi(x, y, z) e^{-i(k_x x + k_y y)} + \int_{-\infty}^{\infty} dx dy \frac{\partial^2}{\partial z^2} \Phi(x, y, z) e^{-i(k_x x + k_y y)} = 0, \quad (30)$$

which reduces to the transformed Laplace equation,

$$\frac{\partial^2}{\partial z^2} \tilde{\Phi}(k_x, k_y, z) = k^2 \tilde{\Phi}(k_x, k_y, z), \quad (31)$$

where $\tilde{\Phi}(k_x, k_y, z)$ is the two-dimensional transform of $\Phi(x, y, z)$, and $k^2 = k_x^2 + k_y^2$. Equation (31) has the general solution

$$\tilde{\Phi}(k_x, k_y, z) = A(k_x, k_y) e^{-kz} + B(k_x, k_y) e^{+kz}, \quad (32)$$

to which we apply the boundary conditions on the bottom and top electrodes specific to solving the weighting potential,

$$\tilde{\Phi}(k_x, k_y, 0) = \tilde{\Phi}_0(k_x, k_y), \quad (33)$$

$$\tilde{\Phi}(k_x, k_y, L) = 0.$$

Here, $\tilde{\Phi}_0(k_x, k_y)$ represents the potential distribution on the pixel plane with one pixel electrode held at unit potential and the rest held at ground potential. The boundary conditions impose constraints,

$$A(k_x, k_y) + B(k_x, k_y) = \tilde{\Phi}_0(k_x, k_y), \quad (34)$$

$$A(k_x, k_y) e^{-kL} + B(k_x, k_y) e^{-kL} = 0,$$

which are readily solved for A and B ,

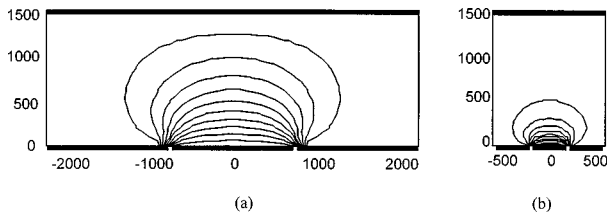


FIG. 2. Weighting potentials shown in cross section through the pixel center. (a) Pixel with 1:1 aspect ratio, $W=1500 \mu\text{m}$. (b) Pixel with 1:4 aspect ratio, $W=375 \mu\text{m}$.

$$A(k_x, k_y) = \frac{\tilde{\Phi}_0(k_x, k_y)e^{+kL}}{[e^{+kL} - e^{-kL}]}, \tag{35}$$

$$B(k_x, k_y) = \frac{-\tilde{\Phi}_0(k_x, k_y)e^{-kL}}{[e^{+kL} - e^{-kL}]}.$$

Substitution into Eq. (32) yields

$$\begin{aligned} \tilde{\Phi}(k_x, k_y, z) &= \tilde{\Phi}_0(k_x, k_y) \frac{e^{kL}e^{-kz} - e^{-kL}e^{+kz}}{e^{kL} - e^{-kL}} \\ &= \tilde{\Phi}_0(k_x, k_y) \frac{\sinh k(L-z)}{\sinh kL}. \end{aligned} \tag{36}$$

This equation provides a convenient way to find the potential at any plane z given the value at the pixel plane, $z=0$, and the constraint that $\Phi=0$ at $z=L$. The method is to find the Fourier transform of Φ_0 , multiply by the propagation function $\sinh k(L-z)/\sinh kL$, and take the inverse transform to obtain the weighting-potential $\Phi_0(x, y, z)$. Figure 2 shows examples of weighting potentials for the case of two pixels with different aspect ratios (pixel width W as compared to detector thickness L). The three-dimensional weighting potentials are displayed in a cross section running through the center of a row of pixels.

The expression in Eq. (36) is similar to that derived by He using an expansion into basis functions.¹⁶ We also note that the technique employed here is equivalent to the angular-spectrum method used in optics for computing diffraction patterns¹⁷ when taken to the electrostatic limit of zero frequency.

B. Analytic solution for a strip electrode geometry

In practice, the Fourier-transform steps described in the previous section must be done numerically for most problems of interest. For the two-dimensional case of a strip detector with no gaps between strips, a simple closed-form expression for the weighting potential can be found. In this case, the weighting potential at the pixel plane is a one-dimensional function,

$$\Phi_0(x) = \text{rect}\left(\frac{x}{W}\right), \tag{37}$$

where W is the strip width. Rather than transforming, multiplying, and inverse transforming, we instead use the convolution theorem for Fourier transforms and convolve with the transform of the propagation function, which is¹⁸

$$\mathcal{F}^{-1}\left\{\frac{\sinh k_x(L-z)}{\sinh k_x L}\right\} = \frac{1}{2L} \frac{\sin \frac{\pi z}{L}}{\cosh \frac{\pi x}{L} - \cos \frac{\pi z}{L}}. \tag{38}$$

The convolution yields

$$\begin{aligned} \Phi_w(x, z) &= \frac{1}{\pi} \left\{ \tan^{-1} \left[\coth \frac{\pi}{2} \left(x - \frac{W}{2}\right) \tan \frac{\pi z}{L} \right] \right. \\ &\quad \left. - \tan^{-1} \left[\coth \frac{\pi}{2} \left(x + \frac{W}{2}\right) \tan \frac{\pi z}{L} \right] \right\}. \end{aligned} \tag{39}$$

This weighting potential is plotted in Fig. 3 for strip electrodes of two different widths.

C. Numerical solution in three dimensions

No closed-form solution will represent the weighting potential for an arbitrary pixel shape, but we can find a general expression that may be evaluated numerically for any pixel geometry of interest. As was done for the two-dimensional case above, we will convolve the pixel area with the Fourier transform of the propagation function. The propagation function, Eq. (36), is radially symmetric in (two-dimensional) k space, and its Fourier transform is a zero-order Hankel transform. The series solution for this transform is¹⁹

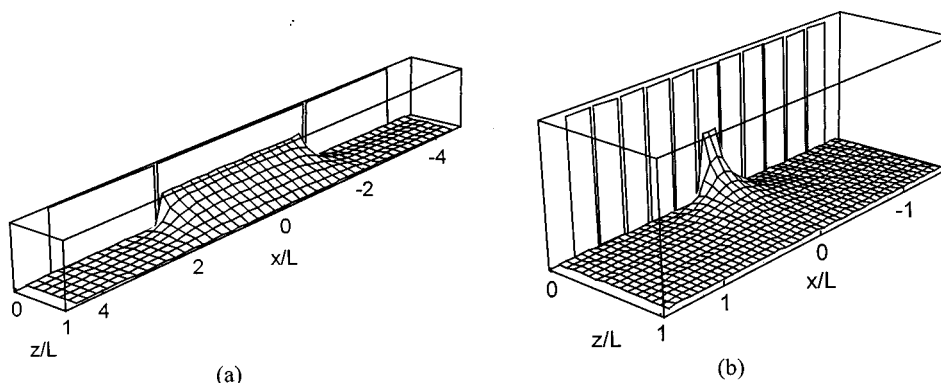


FIG. 3. Weighting potential for strip detectors. For reference, the strips are rendered on the back surface of the plots. (a) Strip width of 5.25 mm for an aspect ratio of $W/L=3.5$. (b) Strip width of 0.375 mm for an aspect ratio of $W/L=0.25$.

$$\frac{1}{2\pi} \int_0^\infty dk k J_0(kr) \frac{\sinh k(L-z)}{\sinh kz} = \frac{1}{L^2} \sum_{n=1}^\infty n \sin\left(\frac{\pi n z}{L}\right) K_0\left(\frac{\pi n r}{L}\right), \quad (40)$$

where $r^2 = x^2 + y^2$. We wish to convolve Eq. (40) with the pixel-plane potential function $\Phi_0(\mathbf{r})$, which takes on unit value inside the pixel boundaries and zero outside. Two-dimensional convolution with the propagation function is written as

$$\Phi_w(\mathbf{r}, z) = \int_{\text{pix}} d^2r' h(\mathbf{r} - \mathbf{r}', z) = \frac{1}{L^2} \int_{\text{pix}} d^2r' \sum_{n=1}^\infty n \sin\left(\frac{\pi n z}{L}\right) K_0\left(\frac{\pi n |\mathbf{r} - \mathbf{r}'|}{L}\right). \quad (41)$$

If, on the other hand, we try to calculate the weighting potential in terms of Green functions using Eq. (28) and the Green function of Eq. (16), we obtain exactly the same form.

V. EFFECT OF CARRIER TRAPPING

If no carriers were trapped as they drifted across the detector, a pixel detector would always register the full-strength signal, proportional to the number of electron-hole pairs created in the gamma-ray absorption. There would be no variation with interaction depth, and no variation with lateral position within the boundary of a pixel. Interactions outside the pixel boundary would produce no signal (assuming there are no spreading effects, such as diffusion, that would cause carriers to move laterally). In the real world, CdZnTe and other compound semiconductor materials that are used as gamma-ray detectors have always been plagued with carrier traps. Even though material quality has steadily improved over the last decade, trapping, especially of holes, remains a major impediment to attainment of good energy resolution in planar detectors. Typical values of the mean-drift length, $\lambda = \mu\tau\mathcal{E}$ at a nominal field strength of $\mathcal{E} = 1000 \text{ V/cm}$ (μ is the carrier mobility and τ is the trapping time) are 2 cm for electrons and 0.02 cm for holes. In this instance, electrons traveling across a 2 mm thick detector will lose less than 10% of their population. When holes are made to travel the same distance only one in 22 000 will make it to the other side. In single-element detectors, where the signal depends only on the total distance that carriers of both signs travel, it is the difference in drift lengths that causes the tail in the pulse-height spectrum. If electrons had the same drift length as holes, the average signal would be weak, but all the pulses would be the same height.

In multipixel detectors, the signal can be calculated using the weighting potential as in Eq. (21). The signal at any given time is the sum of signals due to the presence of all carriers in the detector volume, whether in motion, trapped in the bulk, or recombined at the electrodes. At first, when a small cloud of electron-hole pairs is created at location $\mathbf{r}_i = (x_i, y_i, z_i)$, positive and negative carriers cancel each other out, and the net charge distribution is zero. As the packets of

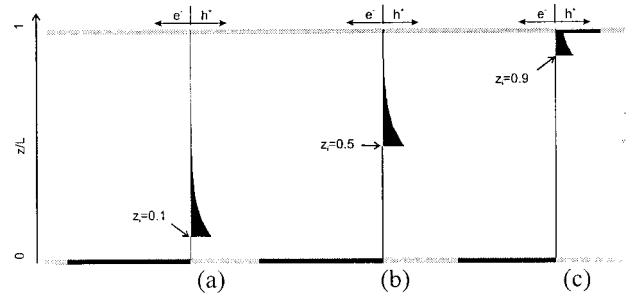


FIG. 4. Final charge distribution in the detector volume, shown for three interaction depths. The number of carriers that have drifted to the electrodes is represented in the figure by the length of the horizontal bars. (a) Interaction near pixel plane at $z/L=0.1$. Nearly all electrons have reached the pixel plane, while nearly all holes are trapped in the medium. (b) Interaction in middle, at $z/L=0.5$. Most electrons reach the pixel plane and most holes are trapped. (c) Interaction near the top, at $z/L=0.9$. Most electrons still reach the pixel plane, while a fraction of the holes have reached the top electrode.

carriers move in opposite directions under the applied bias field, some charge is left behind in deep traps. We assume a simple trapping model with one characteristic trap time for each carrier type and no detrapping. More realistic models of charge distributions include the effects of carrier diffusion and Coulomb repulsion between like charges. After all carriers have had time to drift across the detector, the charge distribution in the detector volume is given by

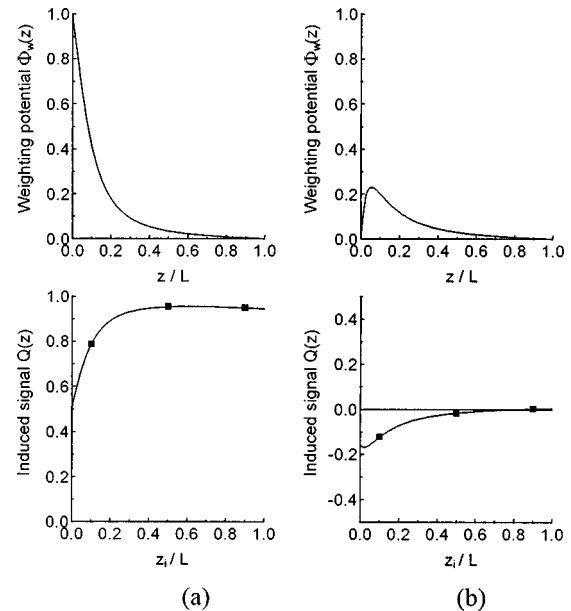


FIG. 5. Weighting potential and expected signal as a function of interaction depth. (a) Weighting potential (top) and final signal strength (bottom) for interactions in the center of a $375 \mu\text{m}$ pixel. Dots in the lower plot correspond to the interaction depths of $z_i=0.1, 0.5,$ and 0.9 whose charge distributions are plotted in Fig. 4. (b) Weighting potential (top) and final signal strength (bottom) for interactions just outside the pixel boundary. A negative pulse results for most interaction depths except those very near the front electrode. The electric field across the $L=1500 \mu\text{m}$ thick detector is 1000 V/cm with the continuous electrode biased negative with respect to the pixel plane. The electron drift length is, $\mu_e\tau_e\mathcal{E}=2.3 \text{ cm}$, and hole drift length is $\mu_h\tau_h\mathcal{E}=0.018 \text{ cm}$.

$$\rho(z; z_i) = \begin{cases} \frac{1}{\lambda_e} e^{-(z_i-z)/\lambda_e} + e^{-z/\lambda_e} \delta(z), & 0 \leq z \leq z_i, \\ -\frac{1}{\lambda_h} e^{-(z-z_i)/\lambda_h} - e^{-(L-z)/\lambda_h} \delta(z-L), & z_i \leq z \leq L. \end{cases} \quad (42)$$

The exponential terms in Eq. (42) represent the trail of trapped charges, and the delta functions represent the remaining untrapped charges that drifted to the electrodes. In the negative-bias configuration we are considering, the electron distribution is given positive value and the hole distribution is assigned negative value. These charge distributions are illustrated in Fig. 4 for three interaction depths.

The net charge signal sensed in the readout circuit is obtained by multiplying the weighting potential by the charge distribution (both polarity carriers) and integrating over the detector volume. Since we have assumed that charges move only in the z direction, the integral reduces to one dimension,

$$Q_{\text{pix}}(z_i) = \int_0^L dz \Phi_w(z) \rho(z, z_i). \quad (43)$$

Figure 5 demonstrates the method of calculating the signal Q_{pix} from the weighting-potential Φ_w using the charge distribution plots of Fig. 4. On the top row of Fig. 5 are plotted weighting potentials for interaction positions in the center of a pixel (a) and just outside the edge of the pixel (b) as a function of the interaction depth z/L . On the bottom row the resulting signal strengths are plotted. Each point on the lower graphs is found by calculating the final profile of trapped and untrapped charge from Eq. (42), multiplying by the weighting-potential curve, and integrating the result. The three points marked on the lower graphs correspond to the example charge distribution of Fig. 4. When the interaction position is within the pixel boundaries, as in Fig. 5(a), the weighting potential has unit strength on the pixel plane, at $z=0$, which is where most of the electrons end up. The negative-valued distribution of trapped holes causes some lowering of the signal for interactions near the pixel electrode but, in this example, has little effect above $z_i/L \cong 0.2$. When the interaction falls just outside the pixel boundary, as in Fig. 5(b), the weighting potential is zero at the $z=0$ plane, and the electron distribution, still largely clustered at the pixel plane, counts for nothing. At interaction depths near the pixel plane, the distribution of trapped holes, scaled by a small weighting potential, results in a net *negative* signal in the readout circuit.

Figure 6 shows the variation of the signal Q_{pix} with lateral position for two interaction depths: at the pixel plane $z=0$ (a), and at the top electrode plane, $z=L$ (b). In the latter case, the signal is strong inside the pixel boundaries, and nearly zero outside the boundaries. In the case shown in Fig. 6(a), the variation in signal within the pixel and the negative signal outside the pixel are due largely to the contribution of the trapped holes.

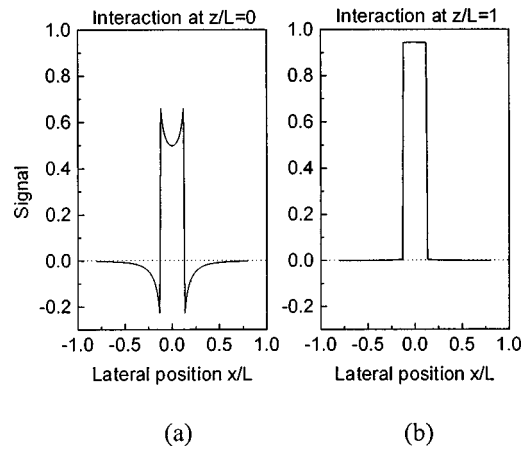


FIG. 6. Lateral variation in the induced signal. (a) Interaction at the pixel plane. (b) Interaction at the top electrode. The experiment being simulated is a thin beam alpha particle being scanned across a $380 \mu\text{m}$ pixel, along the x axis. There is no gap between the pixel pad and surrounding pixels. Material parameters used are the same as in Fig. 5.

VI. THE NEAR-FIELD EFFECT

A consequence of the theory of charge transport in multielement detectors is the realization that the signal induced in a pixel electrode is not independent of the location of the carriers, nor is it constant in time.²⁰ A strong signal is induced in a pixel electrode only when carriers move within a hemispherical region, roughly the size of the lateral pixel dimensions, where the weighting potential is strong. This so-called *near-field* region is apparent in the weighting-potential plots of Fig. 2, and in the upper graph of Fig. 5(a). Outside of this region, motion of charge carriers induces little signal.

The near-field concept provides a convenient framework for explaining charge-transport effects in pixel detectors. For example, the temporal form of the developing signal pulse can be deduced from the shape of the weighting-potential curve. The signal at any time is found from Eq. (43), with the moving charge distribution $\rho(z, z_i)$ evaluated at the given time. If only electron transport is considered, where trapping can be neglected, the packet of electrons can be approximated as the moving delta function $\rho_e(z, z_i) = \delta(z_i + v_e t)$. The (normalized) signal at time t takes the value of the weighting potential at point $z_i - v_e t$. A small-pixel, electron-only signal should follow the shape of the weighting-potential curve, rising very slowly until the electrons are close to the pixel electrode; then sweeping upwards sharply. If the electrons are caused to move away from the pixel electrode by reversing the polarity of the bias voltage, the signal should look like the previous case in reverse, rising steeply at first, then tapering off as the electrons move out of the near-field region. On the other hand, if we consider a large pixel whose near-field region extends across the detector, we would expect the signal to rise more gradually.

The limiting case of an infinite-size pixel is equivalent to a single-element detector. The traditional way to think about signals from single-element detectors is to assume that the current flow is proportional to the number and speed of the carriers, regardless of their position, as in Eq. (1). The charge

building up across an integrating capacitor in the readout circuit grows linearly with time, or where trapping is significant, rounds over according to the Hecht relation [as in Eq. (2) with z/λ terms replaced with t/τ]. This same equation arises from the infinite-pixel model, where the weighting potential follows a straight line extending from the pixel to the front electrode. The resulting signal from electron transport rises linearly, except for some rounding over due to trapping. In the infinite-pixel case, the signal should follow the same curve in time whether the carriers are moving toward the pixel or away from it.

When the motion of holes is considered, trapping effects become as important as near-field effects. In the case where holes are starting at the pixel plane and moving away from the pixel, small pixels will give the strongest signal since most of the holes will pass through the near-field region before they are trapped. Larger pixels will end up with lower signals since holes are being trapped as they move through near fields of larger extent. If the bias voltage is reversed from the usual situation and holes are made to move toward a small pixel, the signal will be very weak since few of them are left by the time the charges move to within the near field. In this situation, signals will be higher for larger pixels, where the near field extends farther into the detector, and more untrapped holes are available to induce signal. In the infinite-pixel case, the signal will again be exactly the same regardless of the direction of hole travel.

Differences in pulse shapes between CdZnTe strip detectors of differing widths were first reported by Hamel *et al.*²¹ Simulations of temporal pulse shapes and corresponding experimental observations are discussed in Sec. VII A.

Another effect predicted by the charge-transport theory is the appearance of negative pulses, which represent current flowing “the wrong way” out of a pixel, as mentioned at the end of Sec. V. This should occur when a gamma ray is absorbed just outside the pixel boundary, at a depth near the pixel plane. The phenomenon can be described by reference to the form of the weighting potentials, as is shown pictorially in Fig. 5(b). Another way to view this effect is in terms of current continuity between the front electrode plane and the pixel electrode plane. The experiments presented Sec. VII B confirm that current not sunk by the pixel electrode is taken up by the surround electrode.

The near-field effect has interesting implications for the quality of pulse-height spectra. In most applications the only quantity that is measured for each gamma absorption is the pulse height, and large numbers of pulse-height measurements are histogrammed to form a pulse-height spectrum. Ideally, a monoenergetic beam of gammas would produce a delta-function pulse-height spectrum in which all the counts fall within a single bin of a multichannel analyzer. This would happen if the pulse heights were the same for all interaction depths (and all lateral interaction locations). Figure 7 shows the relationship between pulse height, interaction depth, and pixel size. In the largest pixels, the pulse height varies nearly linearly with interaction depth. In this regime, the pulse height depends only on the distance that the carriers travel. Since holes are strongly trapped, the signal is generated almost entirely by motion of electrons and is strongest

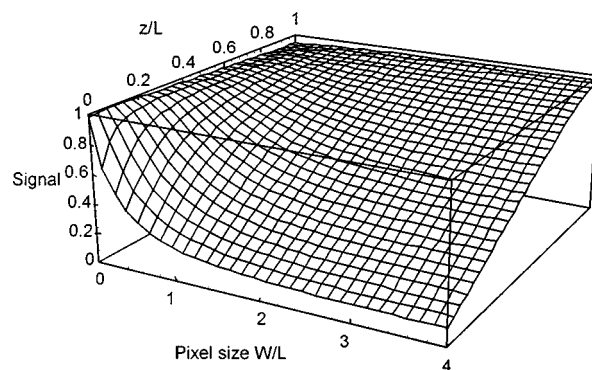


FIG. 7. Induced signal (vertical axis) as a function of pixel size and depth of interaction. For large pixels, the variation of signal with interaction depth is nearly linear. For small pixels, there is only a small variation with interaction depth except near the pixel electrode.

when the electrons have the farthest to travel. On the other end of the pixel-size scale, the pulse height depends only on the number of carriers that come within the near field of the pixel. In the small-pixel limit, the curve is also nearly linear, but the incline is much shallower and slopes in the opposite direction. In this case, the signal strength depends only on how many electrons are trapped before making it to the pixel electrode.

Figure 8 shows an overhead view of the pulse-height plot of Fig. 7. The central line plots the interaction depth that results in the maximum pulse height for a given pixel size. This peak value falls at the point where the optimal balance is struck between the distance the electrons travel and the proximity of the holes to the pixel electrode. On either side of the peak line are lines that delineate a region of interaction depths that result in a pulse height within 2% of the peak. This region gives a qualitative view of the part of the detector that contributes to the photopeak in a pulse-height spectrum. For the material parameters used, the pixel with aspect ratio of $W/L \cong 0.25$ has the largest “good” region. It is interesting to note that pixels can be too small as well as too large. Experimental pulse-height spectra are presented in Sec. VII C.

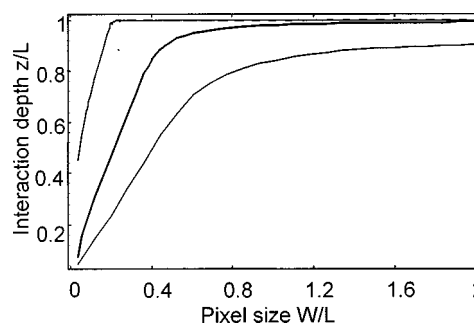


FIG. 8. Optimal interaction depth vs pixel size. The central line shows the interaction depth that gives the peak signal for a given pixel size. The region between the outer lines delineates the range of depths that result in signals within 2% of the peak value. Gamma rays absorbed within this “sweet spot” region will all have pulse heights falling under the photopeak. For the material parameters used in the simulation, a pixel of width-to-length ratio of 0.25 gives the largest photopeak fraction.

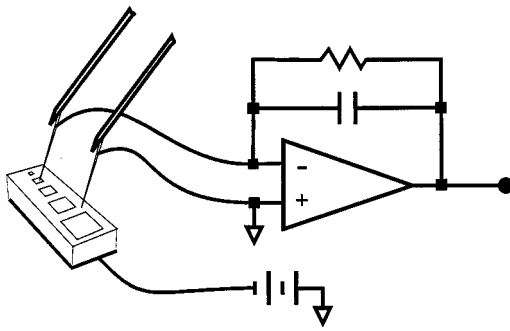


FIG. 9. Point probe test setup. The samples are edge pieces from CdZnTe wafers patterned with test pixel structures ranging in size from $125\ \mu\text{m}$ to $2\ \text{mm}$ on a side. A $25\ \mu\text{m}$ gap separates the pixels from the common surrounding electrode. The test pieces are $1.5\ \text{mm}$ thick and have a continuous “front” electrode on the opposite side. Bias voltage is applied to the front electrode through a conductive rubber pad, which has a hole in it to let alpha radiation through. The pixel and surround electrodes are contacted with point probes with short leads to a preamplifier.

VII. EXPERIMENTAL RESULTS

A series of experiments was performed to confirm the predicted pulse shapes for pixels of various sizes.²² A test-pixel pattern was fabricated on a series of $\text{Cd}_{0.9}\text{Zn}_{0.1}\text{Te}$ slabs, each $1.5\ \text{mm}$ thick. The test pattern consisted of seven square pixel pads ranging in size from 125 to $2000\ \mu\text{m}$, with a $25\ \mu\text{m}$ gap between the pixel and the surrounding electrode. The test pixels could be operated as detectors by contacting the pixel pad and the surround electrode with tungsten or gold point probes, as shown in Fig. 9. In the experiments, both the pixel and surround were held at ground potential either directly or through the summing node of a charge-sensitive preamplifier. In the following, the patterned side of the detector will be referred to as the *back* electrode, while the continuous electrode, to which the bias voltage is applied, will be called the *front*.

A. Temporal pulse shapes

Alpha radiation was used to observe separately the transport of electrons and holes. A $5.1\ \text{MeV}$ alpha from ^{239}Pu is absorbed within the first $20\ \mu\text{m}$ in CdZnTe. At this shallow depth, the carriers of the sign that drift to the near electrode do so within a few nanoseconds; the observed current flow is then due almost entirely to motion of those carriers that drift toward the opposite electrode. Pulses from the charge-sensitive preamplifier were captured by a digitizing oscilloscope at sampling intervals as short as $5\ \text{ns}$. The range in energies of the alpha particles incident on the detector was rather broad, resulting in significant variation in the observed pulse heights. Since we were interested in observing the shape of the pulses rather than the absolute pulse height, the digitized wave forms were renormalized to unit height. This process, shown in Fig. 10, facilitated averaging of successive wave forms to reduce electronic noise. A base-line period before the pulse and a saturation period after the pulse were identified. The mean value within these regions determined the overall pulse height, and all pulses were rescaled in amplitude and were also shifted horizontally so that the mid-points matched. When superimposed on a graph, wave forms processed this way generally lay right on top of one another

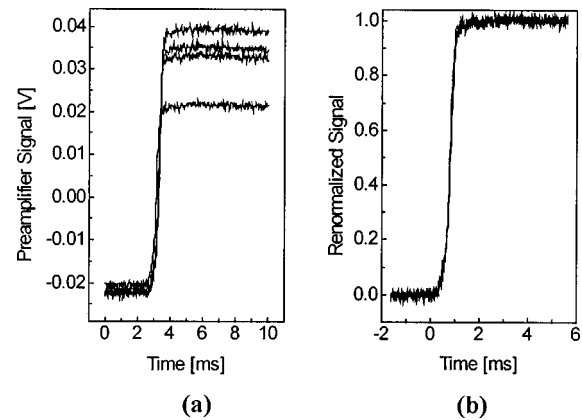


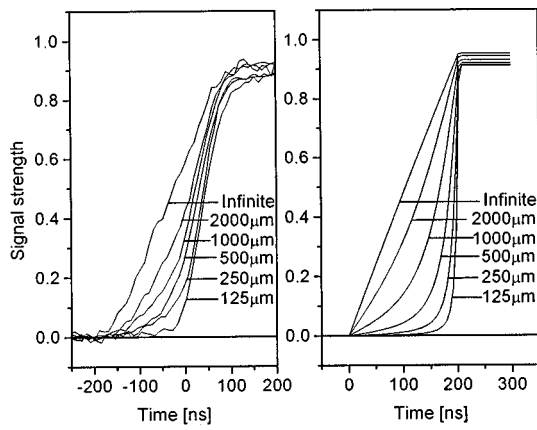
FIG. 10. Averaging of multiple traces. (a) Wave forms as captured by a digital oscilloscope show differences in base-line voltage and start time, as well as variations in pulse height due to the range of energies in the alpha source. (b) After base-line correction, alignment on the time axis, and normalization to final pulse height, successive pulses show the same underlying shape and may be averaged to improve the signal-to-noise ratio.

except for occasional rogue pulses arising from hits near the pixel edge. In the pulse shape studies plotted in Figs. 11 and 12, the traces shown are usually averages of four successive pulses. After averaging, the wave forms were rescaled again to match the pulse height in the corresponding theoretical plot.

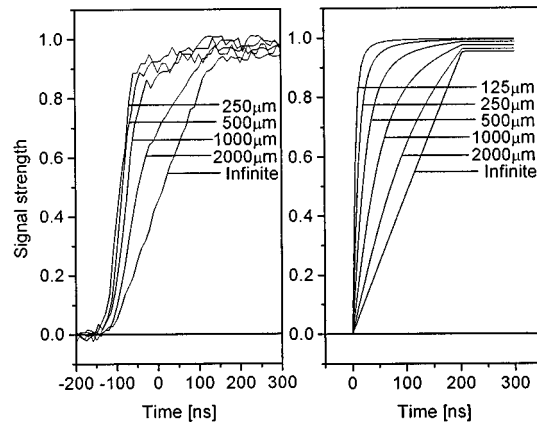
The four combinations of electron/hole transport and front/back irradiation were studied. In each case, the trend of pulse shape as a function of pixel size follows the expected theoretical result. The theoretical plots shown on the right side of Figs. 11 and 12 were generated using the image charge formulation of Eq. (18), but evaluated at time $t < t_{\text{max}}$. In the model, the alpha particles were assumed to interact in the center of a circular pixel. This approximation is generally valid, as pulse shapes do not vary significantly if the interaction point varies laterally within the pixel boundaries. In the theoretical curves only signal induction effects are included. Several other phenomena would tend to slow down and smooth the theoretical curves if taken into account. Chief among these effects are scattering of the secondary particles from the point of initial interaction, diffusion, and Coulomb repulsion of the liberated charges, and trapping of trapped charges.

In Fig. 11 the induced signal from motion of electrons is shown. Since few electrons are trapped during transit across the detector, the signals show the near-field effect clearly, with little interference from trapping. A small variation in final pulse height is due to electron trapping. For electrons moving toward the pixel plane in Fig. 11(a), the smaller pixels have a lower final pulse height because the moving packet of electrons has lost a few percent of its charge before inducing the signal when the packet nears the pixel electrode. When electrons are moving away from the pixel plane as in Fig. 11(b), smaller pixels have a higher pulse height, as the signal has been generated early, before any trapping has taken place.

In the case of an infinite pixel (or a single element), the signal follows the Hecht formula, rounding over slightly. As expected from symmetry, the shape of this curve is exactly the same whether electrons are moving back to front in Fig.



(a)

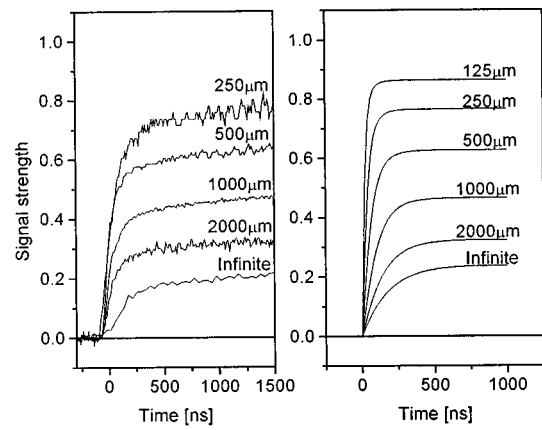


(b)

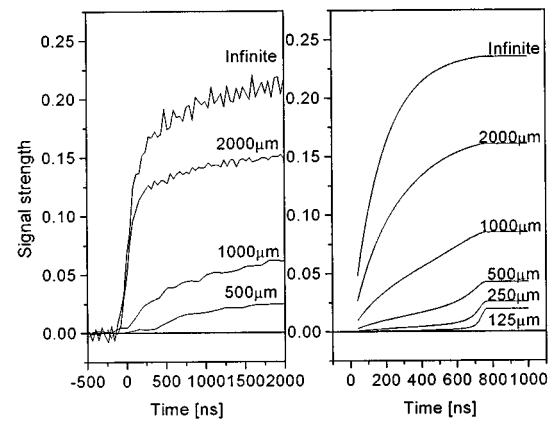
FIG. 11. Experimental (left) and theoretical (right) pulse shapes for electron transport as sensed through pixel electrodes of various size. (a) Alpha radiation is incident on the front electrode; a bias voltage of -100 V moves electrons toward the pixel electrode. (b) Alpha radiation is incident on the pixel electrode, a bias of $+100$ V on the front electrode moves electrons away from the pixel. No experimental trace appears for the smallest pixel because the probe tip used to make electrical contact blocked the incident radiation. In both (a) and (b) rise times are faster for smaller pixels, but the final pulse heights vary only slightly due to the minimal trapping of electrons.

11(a), or front to back in Fig. 11(b). In pixels of finite size the signal is strongest and rise time fastest when the electrons are near the pixel electrode. The curves bend concave up for the front-to-back motion and concave down for the back-to-front motion, with the pulse shapes for a given pixel being nearly symmetrical in time.

Figure 12 shows the case of hole transport. Here, trapping dominates over pixel-size effects. Whether moving back to front in Fig 12(a) or front to back in Fig 12(b), all curves round over due to trapping, with only a small upward swing for the smaller pixels in Fig. 12(b), which was too subtle to observe in practice. The main feature of the hole transport curves is the difference in final pulse height. When holes travel front to back, most are trapped before they reach the near field of the pixel. This effect is most prominent for the smallest pixels. When holes start out at the pixel surface and move away from it, many can contribute significantly to



(a)



(b)

FIG. 12. Experimental (left) and theoretical (right) pulse shapes for hole transport as sensed through pixel electrodes of various size. (a) Alpha radiation is incident on the pixel electrode; a bias of -300 V applied to the front electrode moves holes away from the pixel. The rise time is fastest and pulse height strongest for the smaller pixels, where holes have a chance to move within the near field before they are trapped. No experimental curve appears for the smallest pixel as incident alpha particles were blocked by the probe tip. (b) Alpha radiation is incident on the front electrode; a $+300$ V bias moves holes away from the front electrode. Note the smaller vertical scale than the other plots. No experimental curves are shown for the two smallest pixels as the signal was too weak to be captured.

the signal before they are trapped, and this effect also is strongest in the smallest pixels. This means that the final pulse height for back-to-front hole transport is higher for small pixels and is the main reason why the pulse-height spectrum is much improved in the small-pixel case.

In Fig. 12 there is a disparity in time scale between the theoretical and experimental curves. Observed motion of holes was significantly slower than predicted by the model, which used values of μ_h and τ_h extracted from measurements of pulse height versus bias voltage. At this time we do not have a satisfactory explanation for the observed slow rise times.

B. Signals in surrounding pixels

The principle of current continuity requires that, at any moment in time, the current flowing into the detector through

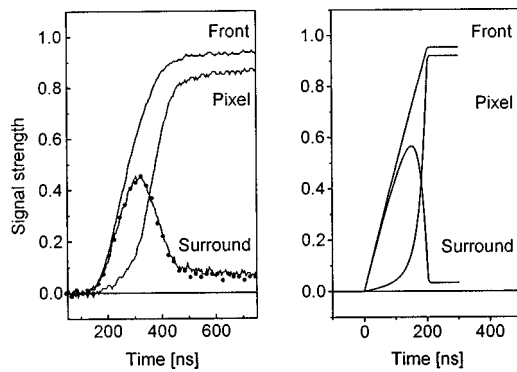


FIG. 13. Continuity of electron currents: measured signals on the left, simulation on the right. The signal from an alpha particle incident on the front electrode opposite a $500\ \mu\text{m}$ pixel is sensed simultaneously in the front electrode, the pixel, and the surround. The (●) symbols plot the mathematical subtraction of the pixel signal from the front signal, which lies, as expected, right on top of the surround signal plot.

the front electrode must equal the sum of currents flowing out of the detector through all of the pixel electrodes. In Figs. 13 and 14 this effect is demonstrated for electron and hole currents on a $500\ \mu\text{m}$ pixel. In this set of experiments, three charge-sensitive preamplifiers were used to simultaneously measure the signal in the pixel, the surround, and the front electrode. The preamplifiers were calibrated to the same responsivity and time delay. The traces shown are from a single alpha absorption; no averaging of curves was performed. In the case of electron flow from front to back, the integrated current through the front electrode is always higher than the pixel signal, with the final pulse height ending up only slightly higher than the pixel pulse height, the difference being due to trapping of electrons. The measured surround signal faithfully follows the difference between the front and pixel signals, as can be seen by the plot of this difference signal which falls on top of the measured curve. In Fig. 14 signals due to hole transport from back to front are illustrated. In this case, the pixel signal is stronger than the front signal, and the difference measured in the surround is negative.

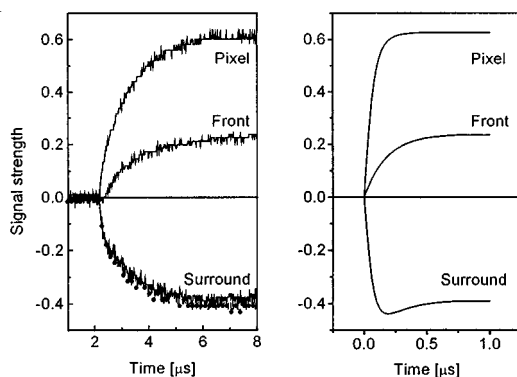


FIG. 14. Continuity of hole currents: measured signals on the left, simulation on the right. The signal from an alpha particle incident on the $500\ \mu\text{m}$ pixel electrode is sensed simultaneously in the front electrode, the pixel, and the surround. The (●) symbols plot the mathematical subtraction of the pixel signal from the front signal, which lies, as expected, right on top of the surround signal plot.

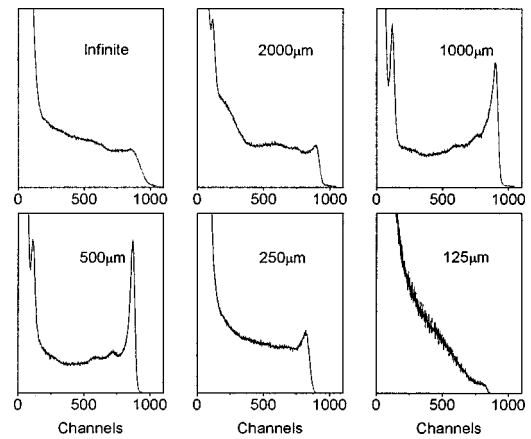


FIG. 15. Pulse-height spectra of $140\ \text{keV}$ gamma rays from $^{99\text{m}}\text{Tc}$ incident on the front electrode. Bias is $-150\ \text{V}$ applied to the front electrode. Pulses from the preamplifier were processed by a spectroscopy amplifier with a $2\ \mu\text{s}$ shaping time, then digitized by a multichannel analyzer. The plots have been scaled vertically to contain equal counts in a window above $30\ \text{keV}$. Spectral quality is best for the midsize pixels. Larger pixels suffer from trapping of holes, while smaller pixels show the effect of charge sharing between the pixel and the surrounding area.

C. Pulse-height spectra

Figure 15 shows pulse-height spectra for six pixel sizes. The spectra were taken with $140\ \text{keV}$ gammas from a $^{99\text{m}}\text{Tc}$ flood source impinging on the front electrode, which was held at $-150\ \text{V}$. Since gamma rays interact at all depths within the detector, a range of pulse heights will result. When a histogram of a large number of pulse heights is plotted as a pulse-height spectrum, some qualitative observations can be made about the spectral and spatial resolution of the detector. Two general trends are apparent in the plots. The highest quality spectra—those showing well-defined photopeaks and the largest photopeak fractions—lie in the middle range of pixel sizes. Larger pixels show the tail characteristic of hole trapping. In the smaller pixels, charge spreading becomes significant, which causes two features in the spectrum. Gamma rays initially absorbed within the pixel boundary, but whose interactions lead to charge being deposited in surrounding regions, cause a tail in the spectrum to the left of the photopeak. Escape of K -shell x rays is the farthest ranging of the mechanisms of nonlocal charge deposition. A characteristic escape peak shows up in the larger pixels but is overwhelmed by other types of scatter for the smaller pixels. Absorption events that take place outside the pixel boundary, but which result in charge spreading into the pixel region, account for the appearance of a large number of low-energy counts, whose number tapers off toward the higher energies.

VIII. CONCLUSIONS

The induced currents in multielement gamma-ray detectors are seen to arise from changes in surface charge density at the pixel plane, which are due to changes in the potential distribution within the detector volume. This potential is found by solving the Laplace equation with the aid of Green functions. Two versions of the Green function approach, one using an expansion into basis functions and an-

other using and infinite series of image charges, are shown to be equivalent. An alternate route to finding the induced signal is to use the Ramo–Shockley theorem, which reduces the problem to finding a weighting potential. This turns out to be equivalent to the normal derivative of the actual potential in the detector integrated over the pixel area. An easy numerical method is available for calculating the weighting potential at any plane in the volume by propagating it from the known potential at the pixel plane. There is even a closed-form solution for the weighting potential that applies to the two-dimensional case of strip detectors. In all cases, the induced signal is found by multiplying the weighting potential or its equivalent over all charges, trapped or untrapped, within the detector volume.

Plots of induced signal as a function of interaction depth can be used to predict detector performance, including temporal response and the form of the pulse-height spectrum. The predicted temporal pulse shapes have been confirmed with experiments using alpha radiation incident on test structures of various sizes. The predicted phenomenon of negative pulses has also been observed. Pulse-height spectra using gamma radiation confirm the expected trend of reduced trapping effects for smaller pixels, but with attendant interference from charge spreading from neighboring pixels.

It is clear from the analysis and experiments that the signals generated in multielement detectors depend strongly on the electrode geometry. The aspect ratio of the pixel volume (pixel width/detector thickness) determines the relative contribution of electrons and holes to the total signal. By choosing the aspect ratio to be small and the pixel electrode to be the anode, electron-mostly signals are obtained, and the problem of hole trapping becomes largely irrelevant. The induction model predicts the temporal shape of signal pulses, and the signals induced in neighboring pixels. Scattering and charge spreading effects become significant for detectors with fine pixel pitches. These effects must be included in a model that accurately predicts pulse-height spectra in imaging detectors.

ACKNOWLEDGMENTS

The authors are grateful for many helpful discussions with J. M. Woolfenden, D. G. Marks, and K. J. Matherson.

- ¹H. B. Barber, D. G. Marks, B. A. Apotovsky, F. L. Augustine, H. H. Barrett, J. F. Butler, E. L. Dereniak, F. P. Doty, J. D. Eskin, W. J. Hamilton, K. J. Matherson, J. E. Venzon, J. M. Woolfenden, and E. T. Young, *Nucl. Instrum. Methods Phys. Res. A* **380**, 262 (1996).
- ²C. M. Stahle, A. Parsons, L. M. Bartlett, P. Kureczynski, J. F. Krizmanic, L. M. Barbier, S. D. Barthelmy, F. Birsa, N. Gehrels, J. Odom, D. Palmer, C. Sappington, P. Shu, B. J. Teegarden, and J. Tueller, *Proc. SPIE* **2859**, 74 (1996).
- ³J. R. Macri, D. B. Boykin, K. Larson, M. Mayer, M. L. McConnell, and J. M. Ryan, *Proc. SPIE* **2859**, 29 (1996).
- ⁴D. G. Marks, H. B. Barber, H. H. Barrett, E. L. Dereniak, J. D. Eskin, K. J. Matherson, J. M. Woolfenden, E. T. Young, F. L. Augustine, W. J. Hamilton, J. E. Venzon, B. A. Apotovsky, and F. P. Doty, *IEEE Trans. Nucl. Sci.* **43**, 1253 (1996).
- ⁵W. Akutagawa and K. Zanio, *J. Appl. Phys.* **40**, 3838 (1969).
- ⁶J. D. Jackson, *Classical Electrodynamics*, 2nd ed. (Wiley, New York, 1975), p. 44.
- ⁷O. Kellogg, *Foundations of Potential Theory* (Ungar, New York, 1929), p. 230.
- ⁸J. D. Eskin, Ph.D. dissertation, The University of Arizona, Tucson (1997), p. 108.
- ⁹S. Ramo, *Proc. IRE* **27**, 584 (1939).
- ¹⁰W. Shockley, *J. Appl. Phys.* **9**, 635 (1938).
- ¹¹E. Durand, *Electrostatique* (Masson et Cie., Paris, 1966), Vol. II.
- ¹²D. J. Wagenaar and R. A. Terwilliger, *Med. Phys.* **22**, 627 (1995).
- ¹³A. Castoldi, E. Gatti, and E. Rehak, *IEEE Trans. Nucl. Sci.* **40**, 256 (1996).
- ¹⁴D. McAllister, J. R. Smith, and N. J. Diserens, *Computer Modelling in Electrostatics* (Research Studies, Letchworth, Hertfordshire, England, 1985).
- ¹⁵S. Kavadias, K. Misiakos, and D. Loukas, *IEEE Trans. Nucl. Sci.* **41**, 397 (1994).
- ¹⁶Z. He, *Nucl. Instrum. Methods Phys. Res. A* **365**, 572 (1995).
- ¹⁷J. W. Goodman, *Introduction to Fourier Optics* (McGraw-Hill, New York, 1968), p. 48.
- ¹⁸M. R. Spiegel, *Schaum's Outline of Theory and Problems of Complex Variables* (McGraw-Hill, New York, 1964), p. 197.
- ¹⁹I. S. Gradshteyn and I. M. Ryzhik, *Table of Integrals, Series, and Products* (Academic, New York, 1965), Eq. (6.666), p. 728.
- ²⁰H. H. Barrett, J. D. Eskin, and H. B. Barber, *Phys. Rev. Lett.* **75**, 156 (1995).
- ²¹L.-A. Hamel, J. R. Macri, C. M. Stahle, J. Odom, F. Birsa, P. Shu, and F. P. Doty, *IEEE Nuclear Science Symposium and Medical Imaging Conference Record* (1995), Vol. 1, pp. 139–143.
- ²²J. D. Eskin, H. B. Barber, and H. H. Barrett, *Proc. SPIE* **2859**, 46 (1996).